A&A 637, A49 (2020)
https://doi.org/10.1051/0004-6361/202037638
© ESO 2020

Astronomy & Astrophysics

Hydrogen non-equilibrium ionisation effects in coronal mass ejections

P. Pagano[1], A. Bemporad[2], and D. H. Mackay[1]

[1] School of Mathematics and Statistics, University of St Andrews, North Haugh, St Andrews, Fife, Scotland KY16 9SS, UK
e-mail: pp25@st-andrews.ac.uk
[2] INAF – Turin Astrophysical Observatory, Via Osservatorio 20, 10025 Pino Torinese, TO, Italy

Received 1 February 2020 / Accepted 27 March 2020

ABSTRACT

Context. A new generation of coronagraphs used to study solar wind and coronal mass ejections (CMEs) are being developed and launched. These coronagraphs will heavily rely on multi-channel observations where visible light (VL) and UV-EUV (ultraviolet-extreme ultraviolet) observations provide new plasma diagnostics. One of these instruments, Metis on board ESA-Solar Orbiter, will simultaneously observe VL and the UV Lyman-α line. The number of neutral hydrogen atoms (a small fraction of coronal protons) is a key parameter for deriving plasma properties, such as the temperature from the observed Lyman-α line intensity. However, these measurements are significantly affected if non-equilibrium ionisation effects occur, which can be relevant during CMEs.
Aims. The aim of this work is to determine if non-equilibrium ionisation effects are relevant in CMEs and, in particular, when and in which regions of the CME plasma ionisation equilibrium can be assumed for data analysis.
Methods. We used a magneto-hydrodynamic (MHD) simulation of a magnetic flux rope ejection to generate a CME. From this, we then reconstructed the ionisation state of hydrogen atoms in the CME by evaluating both the advection of neutral and ionised hydrogen atoms and the ionisation and recombination rates in the MHD simulation.
Results. We find that the equilibrium ionisation assumption mostly holds in the core of the CME, which is represented by a magnetic flux rope. In contrast, non-equilibrium ionisation effects are significant at the CME front, where we find about 100 times more neutral hydrogen atoms than prescribed by ionisation equilibrium conditions. We find this to be the case even if this neutral hydrogen excess might be difficult to identify due to projection effects.
Conclusions. This work provides key information for the development of a new generation of diagnostic techniques that aim to combine visible light and Lyman-α line emissions. The results show that non-equilibrium ionisation effects need to be considered when we analyse CME fronts. Incorrectly assuming equilibrium ionisation in these regions would lead to a systematic underestimate of plasma temperatures.

Key words. Sun: coronal mass ejections (CMEs) – Sun: corona – magnetohydrodynamics (MHD) – Sun: magnetic fields

1. Introduction

Coronal mass ejections (CMEs) are very dynamic and violent phenomena occurring in the solar corona. Despite continuous observations and monitoring of these events from ground and space over the last decades, their elusive nature still presents a major challenge in solar physics. One of the main reasons is that measuring properties of the embedded plasma is always an arduous task. It is complicated by the optical thinness of the coronal plasma, the high speeds and rapid evolution of the CME, and the rapidly changing temperatures. Due to this, remote sensing observations acquired at different wavelengths are combined and analysed with a number of diagnostic techniques to derive the thermodynamic properties of the coronal plasma ejected in CMEs.

New diagnostic techniques that are currently under development are based on the forthcoming remote sensing observations of the ultraviolet (UV) Lyman-α line emitted from neutral hydrogen atoms. These diagnostics will be applied to future data which will be acquired, for instance, by Metis (Antonucci et al. 2017), a new generation multi-channel coronagraph on board the ESA-Solar Orbiter mission that will observe the solar corona in visible light (VL, polarised and non-polarised components) and in the Lyman-α line at the same time. This will be done through the simultaneous acquisition of observations from a broad-band VL channel (580−640 nm) and a narrow-band one in the UV emission around 121.6 nm, where neutral hydrogen atoms emit the Lyman-α line.

At the same time, other forthcoming missions will investigate the solar corona with UV observations centred on the Lyman-α line (the strongest line in the whole UV coronal spectrum), such as the LST instrument that will fly on board the Chinese ASO-S mission in 2022 (Li et al. 2016). The key strength of these new instruments is the switch to multi-channel observations that will allow for the investigation of plasma properties that have been impossible to access thus far due to the limitation of single channel VL observations.

These new observations will pose unprecedented challenges, because it will be essential to have the proper interpretative tools to obtain accurate derivations of CME properties. For example, the simultaneous observation of VL (mostly photospheric emission scattered by free electrons in the solar corona) and UV Lyman-α (emitted by neutral hydrogen atoms mostly excited by chromospheric radiation) can open up a number of diagnostic possibilities. In a plasma, the intensity of the emissions coming from different ionisation stages of the same atomic species are

connected to the abundance of each ionisation level, and they can thus be a useful proxy for the plasma temperature. On the other hand, the Lyman-α emission from neutral hydrogen atoms can be used to derive the plasma temperatures by estimating the fraction of neutrals once the plasma densities are known from VL data.

These techniques were extensively discussed, for instance, by Susino & Bemporad (2016) who demonstrate, by using SOHO/LASCO and UVCS observations, that CME plasma temperatures can be derived by a direct combination of VL and UV Lyman-α intensities even when neglecting spectroscopic information. Similar data analysis methods were also tested by Bemporad et al. (2018), based on the analysis of synthetic data and under different assumptions mostly related with the integration along the line-of-sight (LOS) through the optically thin plasma. These techniques will likely provide the first ever 2D maps of plasma temperatures inside CMEs in the intermediate corona, and they were also strengthened by the improved methods developed by Bemporad & Pagano (2015) and Pagano et al. (2015a) and can be used to derive the column density of the CME plasma from polarised VL observations. Moreover, because of the Doppler dimming (Noci et al. 1987), the UV Lyman-α emission by coronal atoms also depends on their radial outflow speed, and thus the derivation of temperatures in CMEs also requires the technique recently developed by Ying et al. (2019) to reconstruct the 2D distribution of plasma speed in the CME bodies from a sequence of VL images.

For all of the techniques described above to be accurate, we need to understand how the abundance of various ionisation levels evolves in dynamic events, such as CMEs. In this context, the key question pertains to whether the ionisation equilibrium conditions hold for hydrogen atoms throughout the propagation of CMEs in the solar corona or whether there is instead a significant departure from ionisation equilibrium. The ionisation equilibrium hypothesis corresponds to the assumption that a balance exists between all processes, which causes the stripping of electrons from atoms of a given element with all the recombination processes leading to lower ionisation stages. For a long period, this simplified hypothesis has been made in the analysis of UVCS observations of CMEs and post-CME current sheets in the intermediate corona (see e.g. Raymond et al. 2003; Ciaravella et al. 2006), where ionisation equilibrium was assumed to derive plasma temperatures.

The issue of the ion distribution in plasmas that are involved in dynamic events has puzzled solar physicists for decades, as non-equilibrium ionisation effects can be important in a number of scenarios. Karlický et al. (2004) and Reep et al. (2019) addressed the ionisation of the chromosphere during solar flares. Lee et al. (2019) modelled the non-equilibrium ionisation effects following a heating event due to reconnection and found the locations where these effects can be relevant. Bradshaw & Testa (2019) found that non-equilibrium ionisation effects are relevant during nanoflares. Shen et al. (2017) studied the non-equilibrium ionisation in the solar wind. Martínez-Sykora et al. (2016) describe how the non-equilibrium ionisation affects the formation of IRIS lines. Recently, the ionisation equilibrium assumption was (often tacitly) performed by many authors to derive the 2D distributions of plasma temperatures during CMEs (e.g. Hannah & Kontar 2013; Dudík et al. 2014; Su et al. 2016; Aschwanden 2017; Frassati et al. 2019) from the analysis of EUV images acquired with the multiple filters provided by the AIA telescopes on board SDO. In fact, the applied emission measuring techniques require the construction of synthetic EUV spectra for all lines emitted by different ions in each instrument bandpass at various temperatures in order to derive the instrument temperature responses. These synthetic spectra can only be constructed so far, with numerical codes such as the CHIANTI spectral code (see e.g. Dere et al. 2019, and references therein), by assuming ionisation equilibrium.

On the other hand, departures from ionisation equilibrium are expected to occur in many dynamic phenomena in the solar atmosphere, as suggested by the significant spectral variability observed to occur on timescales shorter than the ion equilibration times. The principles of a numerical tool for the calculation of non-equilibrium ionisation states in the solar corona were illustrated by Bradshaw (2009), and calculations of the ionisation equilibrium timescales have been performed by several authors, such as Smith & Hughes (2010) who derived the ionisation equilibrium timescales in the absence of flows. Recently, Dudík et al. (2017) reviewed the state of the art of these methods. The departure from ionisation equilibrium in CME shocks for oxygen and silicon was justified with a numerical model by Pagano et al. (2008). The violation of the ionisation equilibrium assumption in the post-CME EUV dimming region was reported by Imada et al. (2011) in the higher temperature range. Later Shen et al. (2013) showed that, because of non-equilibrium ionisation effects, the analysis of EUV imaging observations of post-CME current sheets would lead to an under (over) estimate of plasma temperatures at low (high) heights by about a factor of two if equilibrium is assumed. On the other hand, Kocher et al. (2018) reported that in a CME core, departures from ionisation equilibrium were within 10% for hydrogen and helium atoms in the erupting filament. Very recently, possible observational consequences of non-equilibrium ionisation in the EUV imaging of CME related phenomena, such as post-flare arcades and CME-driven shocks, were investigated by Lee et al. (2019): the authors re-analysed previous dynamic events studied with an emission measuring technique applied to EUV and soft X-ray images and they conclude that the temperature of hotter plasma that is not in ionisation equilibrium is lower than the temperature calculated by assuming ionisation equilibrium. These effects can be important, not only for the study of CMEs, but also for elemental abundance determination in stationary solar wind flows (Shi et al. 2019).

Similar analyses have frequently been performed for observations of erupting events in the transition region and in the inner corona ($R < 1.5\,R_\odot$), but not very often for CMEs observed higher up in the intermediate corona during the expansion phase ($R > 1.5\,R_\odot$). At these altitudes, the problem of ionisation equilibrium was discussed, for instance, by Akmal et al. (2001), dealing with UVCS observations of a CME and the reconstruction of the thermal evolution of the observed plasma. More recently Landi et al. (2010) and Murphy et al. (2011) have reported similar observations of CMEs with UVCS spectra and other EUV imagers and spectrometers. In the interpretation of UVCS observations, the problem was also investigated by Ciaravella et al. (2001) with numerical simulations, inferring the plasma heating rate in a CME by assuming ionisation equilibrium. Later, Pagano et al. (2008) simulated the UV spectroscopic emission from a CME (focusing on the evolution during a shock transit) as observed by UVCS by also including the effects of non-equilibrium ionisation. More recently, a non-equilibrium ionisation analysis was performed by Jejčič et al. (2017) to derive the physical parameters of an erupting prominence observed spectroscopically with UVCS. While a significant amount of work has been carried out, none of these works focus on the evolution of neutral hydrogen ionisation states for the analysis of the Lyman-α line intensity evolution observed during CMEs.

Hence in summary, the interpretation of coronagraphic observations of CMEs in the Lyman-α line that will be provided by forthcoming instruments, such as Metis on board Solar Orbiter and LST on board ASO-S missions, will require a deep understanding of which regions in CME bodies can be considered in ionisation equilibrium. In order to answer this question, in this paper we adopt a theoretical approach by using our realistic numerical modelling of the propagation of a CME to study the evolution of the ionisation state of hydrogen atoms during the CME. Through this, we can relate our results with the ionisation state that is prescribed by ionisation equilibrium conditions.

In order to reach our objectives, we started from the magnetohydrodynamic (MHD) simulation of Pagano et al. (2014) of a magnetic flux rope ejection. Magnetic flux ropes are structures found in the solar corona that usually lie on polarity inversion lines (PILs; Cheng et al. 2010) that are known to suddenly erupt and produce CMEs (Chen 2011; Yan et al. 2017; Song et al. 2014; Howard & DeForest 2014). We first used a magnetofrictional model to describe the formation phase of magnetic flux rope using a quasi-static and magnetically dominated approach and we switched to MHD simulations when the magnetic configuration is unstable. In the MHD simulations, we solved the general form of the MHD equations that are appropriate to describe a dynamic evolution where the dominant forces can be magnetic, pressure gradients, or gravity.

Once we solved the MHD equations for the eruption of the magnetic flux rope, we devised a technique to reconstruct the history of the ionisation state of hydrogen atoms in the 3D domain of the MHD equations as a function of time. Such an approach was already successfully adopted by Pagano et al. (2008) for the study of the emission of oxygen and silicon lines in shocks connected with CMEs. In order to reconstruct the ionisation state of hydrogen in our MHD domain, we estimated the advection of neutral and ionised hydrogen atoms and the local rate of ionisation and recombination processes separately. Finally, we combined these two terms to obtain the abundances of neutral and ionised hydrogen atoms as a function of space and time.

The paper is structured as follows. In Sect. 2 we summarise the key properties of the MHD simulation we use here and in Sect. 3 we describe the technique we used to reconstruct the history of the ionisation state of hydrogen atoms. Next in Sect. 4, we illustrate the results of our study and we draw our conclusions in Sect. 5.

2. MHD simulation

In the present paper, we analyse the ionisation state of hydrogen atoms during a CME, starting from the data obtained in the MHD simulation of Pagano et al. (2014). In Pagano et al. (2014), the simulation of magnetic flux rope ejection was carried out by coupling the magnetofrictional model of Mackay & van Ballegooijen (2006) and Mackay et al. (2011) with a MHD simulation. This technique, initiated by Pagano et al. (2013a) and used in a number of studies (Pagano et al. 2013b, 2014, 2015b,a, 2018; Rodkin et al. 2017), has been proven to be effective in modelling the full life span of magnetic flux ropes.

In that simulation, we used the MPI-AMRVAC software (Porth et al. 2014) to solve the MHD equations, where solar gravity, anisotropic thermal conduction, and optically thin radiative losses are treated as source terms:

$$\frac{\partial \rho}{\partial t} + \boldsymbol{\nabla} \cdot (\rho \boldsymbol{v}) = 0, \tag{1}$$

$$\frac{\partial \rho \boldsymbol{v}}{\partial t} + \boldsymbol{\nabla} \cdot (\rho \boldsymbol{v}\boldsymbol{v}) + \nabla p - \frac{(\boldsymbol{\nabla} \times \boldsymbol{B}) \times \boldsymbol{B})}{4\pi} = +\rho \boldsymbol{g}, \tag{2}$$

$$\frac{\partial \boldsymbol{B}}{\partial t} - \boldsymbol{\nabla} \times (\boldsymbol{v} \times \boldsymbol{B}) = 0, \tag{3}$$

$$\frac{\partial e}{\partial t} + \boldsymbol{\nabla} \cdot [(e + p)\boldsymbol{v}] = \rho \boldsymbol{g} \cdot \boldsymbol{v} - n^2 \chi(T) - \nabla \cdot \boldsymbol{F}_{\rm c}, \tag{4}$$

where t is the time, ρ is the density, $\boldsymbol{v}$ is the velocity, p is the thermal pressure, $\boldsymbol{B}$ is the magnetic field, e is the total energy, n is the number density, $\boldsymbol{F}_{\rm c}$ is the conductive flux according to Spitzer (1962), and $\chi(T)$ represents the radiative losses per unit emission measure (Colgan et al. 2008). The thermal pressure p, is expressed in terms of the internal, total, kinetic, and magnetic energy

$$\frac{p}{\gamma - 1} = e - \frac{1}{2}\rho \boldsymbol{v}^2 - \frac{\boldsymbol{B}^2}{8\pi}, \tag{5}$$

where $\gamma = 5/3$ denotes the ratio of specific heat, and the expression for solar gravitational acceleration is

$$\boldsymbol{g} = -\frac{G M_\odot}{r^2}\hat{r}, \tag{6}$$

where G is the gravitational constant, $M_\odot$ denotes the mass of the Sun, r is the radial distance from the centre of the Sun, and $\hat{r}$ is the corresponding unit vector. The spatial domain of this simulation extends over $3\,R_\odot$ in the radial direction starting from $r = R_\odot$. The colatitude, θ, spans from $\theta = 30^\circ$ to $\theta = 100^\circ$ and the longitude, ϕ, spans over 90°. For more details, we refer the reader to a series of works: Mackay & van Ballegooijen (2006), where the initial pre-eruptive configuration was derived using a magnetofrictional model; Pagano et al. (2013a), where, for the first time, we coupled the eruptive initial conditions with the MHD simulations; Pagano et al. (2013b), where we study the effect of gravity on the propagation of CMEs in the corona; and, finally, Pagano et al. (2014) where we included the effects of non-ideal MHD.

In the magnetofrictional model, two neighbouring magnetic bipoles are allowed to evolve under the effect of differential rotation, meridional flows, and surface diffusion. As one of the two bipoles is initially more sheared than the other, a magnetic flux rope forms in the corona above its polarity inversion line (PIL) after 19 days of evolution (Mackay & van Ballegooijen 2006). At the same time and due to the magnetic field configuration, another PIL separates the two bipoles and above this last PIL, a null point is present. With evolution and the formation of a flux rope, the magnetic field configuration obtained is not stable and a significant Lorentz force is present underneath the magnetic flux rope. In this MHD simulation, we also constructed an atmosphere around the magnetic field configuration where the magnetic flux rope was initially modelled to be colder and denser than its surroundings. This was done by imposing a temperature distribution dependent of the θ-component of the magnetic field, so as to have cold plasma where the we have a magnetic flux rope that develops with an θ-directed axial magnetic field in this configuration and, at the same time, maintaining a horizontal thermal pressure balance, so that these cold regions are also denser than their surroundings. In the initial condition of this simulation, the minimum temperature was set to $T_{\rm min} = 10^4$ in a corona at $T = 2$ MK, leading to a magnetic flux rope structure that is up to 200 times denser than the background corona. More details on how this atmosphere was constructed can be found in Pagano et al. (2014).

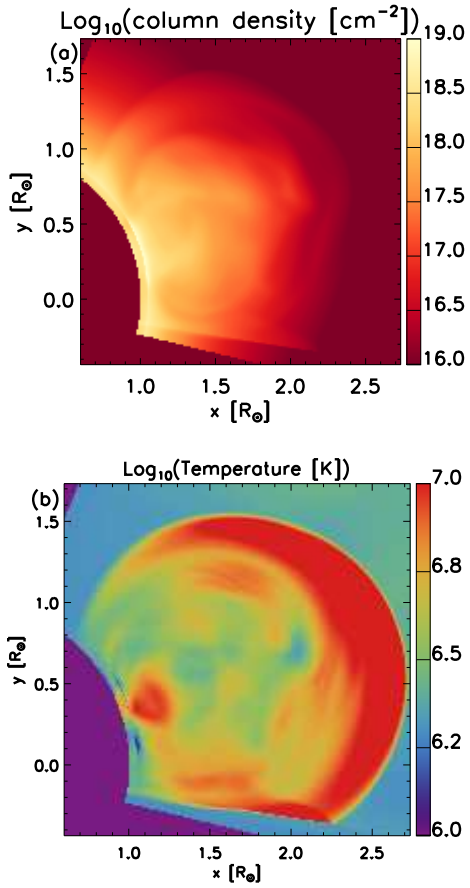

Fig. 1. (*a*) Map of column density and (*b*) map of temperature averaged over plasma density of the simulation at $t = 19.7$ min interpolated in a cartesian frame. We only show the field of view over 1 $R_\odot$.

The flux rope was then ejected out of the corona due to the Lorentz force distribution, which built up over 19 days of evolution. Figure 1 shows the simulation after 19.7 min of evolution for both the column density (Fig. 1a) and the density-weighted temperature along the LOS, $T_{\rm LOS}$ (Fig. 1b)

$$T_{\rm LOS} = \frac{\int_{-\infty}^{+\infty} \rho T \, {\rm d}z}{\int_{-\infty}^{+\infty} \rho \, {\rm d}z}. \tag{7}$$

The key features of this evolution are that we find plasma travelling outwards because of the ejection and the plasma distribution closely resembles a three-component CME, as a dense front is followed by a denser core with a void in between. A similar pattern is found in the temperature map, where we find a hot front of the ejection due to the compression where a colder region lags behind.

One important aspect of the simulation is that the direction along which the magnetic flux rope expands is not radial and, instead, the magnetic flux rope is ejected in the direction of the null point that lies between the two bipoles. Therefore, knowing the direction of propagation as well as the location of the magnetic flux rope and the CME front in this direction as function of time, we can follow the plasma density and temperature inside these structures. Figure 2 shows the density and temperature at the centre of the flux rope and at the CME front as a function of time.

We find that the densities of both the centre of the flux rope and the CME front decrease in time as all structures expand and move into regions of lower density when higher in the solar corona. The evolution of the plasma temperature is instead more complex. As explained in Pagano et al. (2014), the temperature of the magnetic flux rope immediately increases during the very early stage of the MHD simulation due to the conversion of magnetic energy into thermal energy. Later on, as the magnetic flux rope expands adiabatically, it also cools down slowly. The CME front instead shows a constant temperature increase. It basically coincides with the magnetic flux rope at the beginning of the simulation ($t < 6$ min) as the two structures are very close and it is not possible to identify a very distinct CME front. Afterwards, the compression occurring at the CME front heats the plasma to over 10 MK, where it more or less plateaus until the end of the simulation. While a temperature significantly above 10 MK may seem unrealistic in the solar corona, such values are nevertheless in the correct order of magnitude for the tenuous plasma of the outer corona, which is violently heated by the compression generated from a violent CME.

3. Ionisation state of plasma

In this section, we illustrate how we reconstructed the ionisation state of the hydrogen atoms in the plasma as a function of space and time in our MHD simulation. This was done by post-processing the results of the MHD simulation, thus assuming that the ionisation state of hydrogen does not affect the dynamic and thermal evolution of the CME in the MHD simulation. This assumption is based on the fact that the number of neutral hydrogen atoms is usually many orders of magnitude smaller than coronal protons and electrons, and in collisionless plasma even the very few neutral atoms do not interact with other particles via either collisions or magnetic fields. This strategy was already adopted in Pagano et al. (2008) for the derivation of the ionisation state of oxygen and silicon.

In order to reconstruct the ionisation state of hydrogen, we needed to solve the following coupled differential equations

$$\frac{\partial n_{\rm HI}}{\partial t} = -\boldsymbol{\nabla} \cdot (n_{\rm HI} \boldsymbol{v}) + n_{\rm HII} \left(\alpha_{\rm HII} n_{\rm HII} - q_{\rm HI} n_{\rm HI}\right) \tag{8}$$

$$\frac{\partial n_{\rm HII}}{\partial t} = -\boldsymbol{\nabla} \cdot (n_{\rm HII} \boldsymbol{v}) + n_{\rm HII} \left(q_{\rm HI} n_{\rm HI} - \alpha_{\rm HII} n_{\rm HII}\right) \tag{9}$$

where $n_{\rm HI}$ and $n_{\rm HII}$ are the number densities of neutral and ionised hydrogen atoms as function of space and time, $\alpha_{\rm HII}$ is the recombination rate by collisions of ionised hydrogen, $q_{\rm HI}$ is the ionisation rate by collisions of neutral hydrogen, t is the independent variable time, and $\boldsymbol{v}$ is the velocity field that is input from the MHD simulation. As we have the velocity field at the output cadence of the MHD simulation, that is 34.8 s, we linearly interpolated for intermediate times. The values of $\alpha_{\rm HII}$ and $q_{\rm HI}$ were taken from CHIANTI spectral code (Dere et al. 2019) as a function of the temperature T of the plasma and number density $n_{\rm e}$ of the electrons.

The general solution of these equations provides the temporal and spatial dependent abundance of $n_{\rm HI}$ and $n_{\rm HII}$, including solutions that describe the out of ionisation equilibrium configurations. In order to solve these equations, we assumed an initial condition at $t = 0$ where the hydrogen atoms are in ionisation equilibrium as follows:

$$n_{\rm HII} = \rho / m_{\rm p} \tag{10}$$

$$\left[\alpha_{\rm HII} n_{\rm HII} - q_{\rm HI} n_{\rm HI}\right] = 0. \tag{11}$$

Equation (10) expresses that the number of ionised hydrogen atoms is the same as the number density of electrons as described

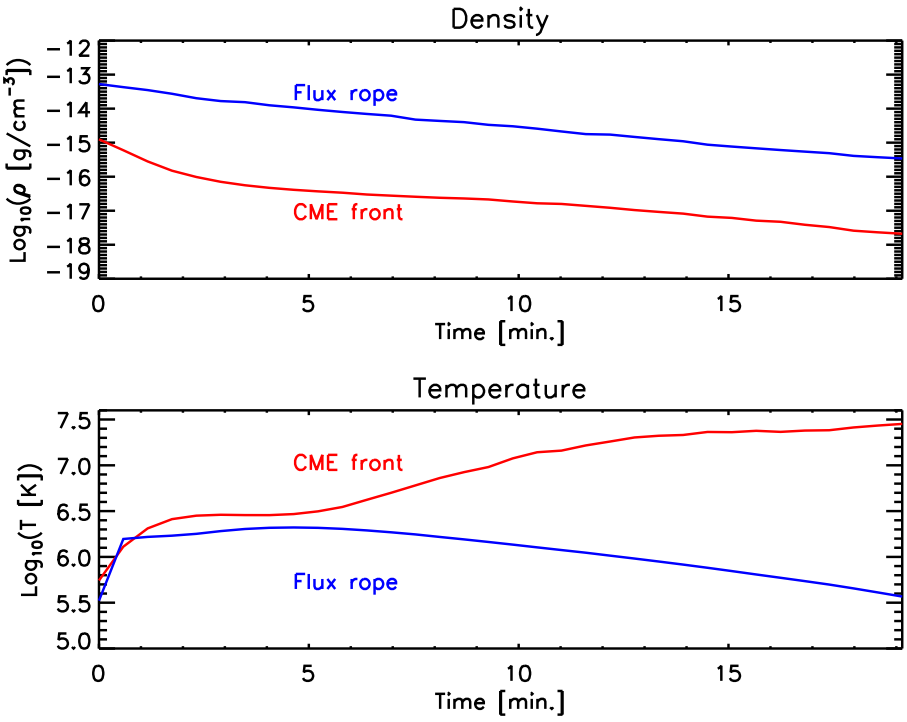

Fig. 2. Time evolution of plasma density (*top panel*) and temperature (*bottom panel*) at the centre of the flux rope (blue line) and at the CME front (red line).

by the MHD equations, and in Eq. (11) we derived the number of neutral hydrogen atoms from the number of ionised hydrogen atoms when the number of recombinations matches the number of ionisations. As the temperature is not uniform at $t = 0$ in our MHD simulation, neither is the ratio $n_{\rm HI}/n_{\rm HII}$.

In order to solve the two differential equations (Eqs. (8) and (9)) that govern the ionisation state of hydrogen, we needed to evaluate the left-hand side of both equations to obtain the rate of change for $n_{\rm HII}$ and $n_{\rm HI}$ as a function of space at a given time t. In order to do so, we assumed that we can split the right-hand side terms of Eqs. (8) and (9) into two terms, the advection term as well as the ionisation and recombination term, and that accordingly we can integrate Eqs. (8) and (9) in time to obtain the finite variation of $n_{\rm HII}$ and $n_{\rm HI}$ over a finite integration time:

$$\Delta n_{\rm HI} = [{\rm ADV_{HI}}] + [{\rm IR_{HI}}] \tag{12}$$

$$\Delta n_{\rm HII} = [{\rm ADV_{HII}}] + [{\rm IR_{HII}}]\,. \tag{13}$$

We then separately evaluated each term on the right-hand side of Eqs. (12) and (13) and added their contributions to evaluate the left-hand side. In the next two sections, we describe how we evaluated the advection terms as well as the ionisation and recombination terms.

3.1. Advection term

The advection term describes the motion of the hydrogen atoms (neutrals and ions) due to the velocity field derived from the solution of the MHD equations. For neutral hydrogen atoms, this term can be written as:

$$[{\rm ADV_{HI}}] = -\boldsymbol{\nabla}\cdot(n_{\rm HI}\boldsymbol{v})\Delta t \tag{14}$$

where Δt is the finite integration time step. In order to estimate $[{\rm ADV_{HI}}]$ and $[{\rm ADV_{HII}}]$, we used an explicit Godunov scheme (Godunov 1959) where we used boundary conditions that are consistent with the ones adopted in solving the MHD equations. In the Godunov scheme, we needed to estimate the flux of ionised $\boldsymbol{F}^{n_{\rm HII}}$ and neutral $\boldsymbol{F}^{n_{\rm HI}}$ hydrogen atoms that cross each face of the finite difference cells of the MHD simulation grid. In order for this explicit scheme to work, we needed to limit the integration time step, Δt, so that the change of the number of neutral or ionised hydrogen atoms due to the fluxes is smaller than the number of atoms in each cell. For instance, considering the r direction and the number density $n_{\rm HII}$, this constraint reads as follows:

$$\Delta t < c_{\rm CFL}\frac{\Delta r}{F_{\rm r}^{n_{\rm HII}}}, \tag{15}$$

where $c_{\rm CFL} < 1$ is a parameter to satisfy the CFL (Courant-Friedrichs-Lewy) condition (Courant et al. 1928). It was chosen to be $c_{\rm CFL} = 0.75$ in this work. We then took the minimum from all of the cells, for all directions, and for $n_{\rm HII}$ and $n_{\rm HI}$ to estimate the integration time Δt. However, because of the high heterogeneity in the initial $n_{\rm HII}$ and $n_{\rm HI}$ distributions and the steep dependence of $\alpha_{\rm HII}$ and $q_{\rm HI}$ on the temperature, the explicit solution of the advection term can lead to values of Δt that are too small for reasonable computational times.

In order to circumvent this problem, we applied two measures. First of all, we used a smoothed distribution of ρ, T, and $\boldsymbol{v}$ as input from the MHD equations, and second we applied a flux limiter for the Godunov scheme. The smoothing simply consists of replacing the values of each quantity at time t in each computational cell with the average among a volume of $3\times3\times3$ cells centred around the same cell. As far as the flux limiter is concerned, we first estimated the Δt resulting from a given distribution of $n_{\rm HII}$, $n_{\rm HI}$, and $\boldsymbol{v}$. If Δt is smaller than 0.1 s in a cell, we redistributed a fraction of 10^{-4} of the number of ionised and neutral hydrogen atoms from that cell to the neighbouring cells. This was iterated until $c_{\rm CFL}\Delta t \geq 0.1$ s. When this condition was satisfied, we picked $\Delta t = 0.1$ s, which is certainly smaller than the Δt required by Eq. (15). This flux limiter is equivalent to a diffusion term that operates on a faster time scale of the advection of the bulk plasma motion, such as turbulence.

3.2. Ionisation and recombination term

The ionisation and recombination term expresses the rate at which neutral or ionised hydrogen atoms change the ionisation state per unit of time. As hydrogen atoms have only two possible ionised states, we can write the following:

$$[\mathrm{IR_{HI}}] = -[\mathrm{IR_{HII}}] = n_{\mathrm{HII}}\left(\alpha_{\mathrm{HII}} n_{\mathrm{HII}} - q_{\mathrm{HI}} n_{\mathrm{HI}}\right)\Delta t. \quad (16)$$

In order to estimate the value of $[\mathrm{IR_{HI}}]$ and $[\mathrm{IR_{HII}}]$, we used an implicit scheme. In this implicit scheme, we set $\Delta t = 0.1$, as we did for the advection term, to ensure that the two terms are integrated over the same time interval. Then, we solved the implicit scheme associated with the finite difference expression for Eq. (16) for $[\mathrm{IR_{HI}}]$ and the corresponding equation for $[\mathrm{IR_{HII}}]$.

This corresponds to solving the system of quadratic equations

$$n_{\mathrm{HI}}^{t+\Delta t} - n_{\mathrm{HI}}^{t} = n_{\mathrm{HII}}^{t+\Delta t}\left(n_{\mathrm{HII}}^{t+\Delta t}\alpha_{\mathrm{HII}} - n_{\mathrm{HI}}^{t+\Delta t} q_{\mathrm{HI}}\right)\Delta t \quad (17)$$

$$n_{\mathrm{HII}}^{t+\Delta t} - n_{\mathrm{HII}}^{t} = n_{\mathrm{HII}}^{t+\Delta t}\left(n_{\mathrm{HI}}^{t+\Delta t} q_{\mathrm{HI}} - n_{\mathrm{HII}}^{t+\Delta t}\alpha_{\mathrm{HII}}\right)\Delta t \quad (18)$$

for $n_{\mathrm{HI}}^{t+\Delta t}$ and $n_{\mathrm{HII}}^{t+\Delta t}$, which are the values for n_{HI} and n_{HII} at the time $t+\Delta t$, whereas n_{HI}^{t} and n_{HII}^{t} are the known values of n_{HI} and n_{HII} at the time t.

In a few cells near the lower boundary of the MHD simulation, where boundary conditions lead to sharp gradients in the number density of ionised and neutral hydrogen atoms or where rapid changes in the plasma temperature occur, it is possible for n_{HII} or n_{HI} to become negative. For this reason, we always imposed ionisation equilibrium over the first ten layers of the computational domain in r, until $r < 1.17\,R_\odot$, and when this happened, we also imposed equilibrium ionisation on other cells to restore a physically meaningful solution. It should be noted that as soon as the magnetic flux rope is ejected from its initial position near the lower boundary at $t = 0$, these locations are no longer relevant for the analysis of the CME ionisation state as the magnetic flux rope is soon located far from the lower boundary where these issues arise.

4. Results

Having solved the MHD equations for a magnetic flux rope ejection and then reconstructed the history of the ionisation state of hydrogen atoms, we now discuss how the abundances of ionised and neutral hydrogen atoms without ionisation equilibrium compare to those derived in the usual hypothesis of ionisation equilibrium. Figure 3 shows the column density of n_{HI} and n_{HII} at $t = 0$ and $t = 19.7$ min from the same point of view as in Fig. 1. In order to display these results in terms of a potential observations, we used a 3D cartesian box, where x is the east-west direction of the Sun, y is the north-south direction, and z is the direction along the LOS. The evolution of both n_{HI} and n_{HII} follow a similar pattern as in Fig. 1, where the distribution of n_{HI} and n_{HII} change significantly as soon as the magnetic flux rope ejection propagates through the corona. There is evidence of the CME three-part structure in the distributions of n_{HI} and n_{HII}.

The key aim of this work is to measure the out-of-equilibrium ionisation effects in different CME components. Therefore, in Fig. 4 we show the difference of the logarithms of the ionisation fraction for the column densities of neutral and ionised hydrogen at $t = 19.7$ min. In these maps, we find positive values when the non-equilibrium ionisation effects lead to a higher cumulative number of neutral or ionised hydrogen

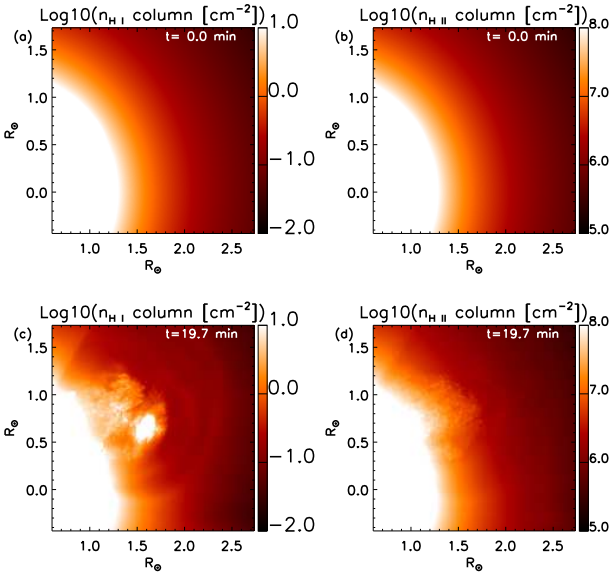

Fig. 3. Column density of neutral hydrogen (maps *a* and *c*) and ionised hydrogen (maps *b* and *d*) at $t = 0$ min and at $t = 19.7$ min, respectively.

atoms compared to that of the ionisation equilibrium condition along the LOS. Negative values occur when the number of neutral or ionised atoms is less than in the equilibrium condition. We find extended regions where non-equilibrium ionisation effects become relevant. This is particularly true for the abundance of neutral hydrogen atoms where differences in the logarithm between the number of atoms and the equilibrium condition along the LOS can be as large as 0.2; whereas for the ionised hydrogen atoms, such differences are less than 10^{-8}, making non-equilibrium ionisation effects rather marginal. In particular, for the abundance of neutral hydrogen, we find that overall there are more atoms of this species along the LOS than prescribed by ionisation equilibrium conditions and only in some small localised regions do we find fewer atoms of this species with respect to ionisation (Fig. 4a).

As non-equilibrium ionisation effects are relevant for neutral hydrogen in particular, we plotted the number density of neutral hydrogen in Fig. 5a at the initial condition, at $t = 14.5$ min, and at $t = 19.7$ min along the direction of propagation of the magnetic flux rope. If we focus on the curve at $t = 19.7$ min, we find that the number of neutral hydrogen atoms increases with respect to the initial conditions where the magnetic flux rope is located ($s \sim 0.7\,R_\odot$), as this structure is colder than the ambient corona travelling upwards, thus carrying a higher abundance of neutral hydrogen atoms through advection. At the same time, the situation is more complex for the CME front ($s \sim 1.6\,R_\odot$) where the number of neutral hydrogen atoms has not changed significantly with respect to the pre-CME corona. The number of neutral hydrogen atoms changes more because of the local temperature variations, that is, ionisation and recombination processes rather than neutral hydrogen atom advection.

In comparing the neutral hydrogen atom abundance with the ionisation equilibrium conditions, the difference is much more evident at the CME front than at the magnetic flux rope location (Fig. 5b). This is clearly visible in the cuts at $t = 14.5$ min and $t = 19.7$ min. At the magnetic flux rope location, the abundance of neutral hydrogen atoms can be more than 10 times higher than those of ionisation equilibrium, but it is also highly variable, and this occurs in extremely localised regions. In contrast, at the CME front, the abundance of neutral hydrogen atoms is

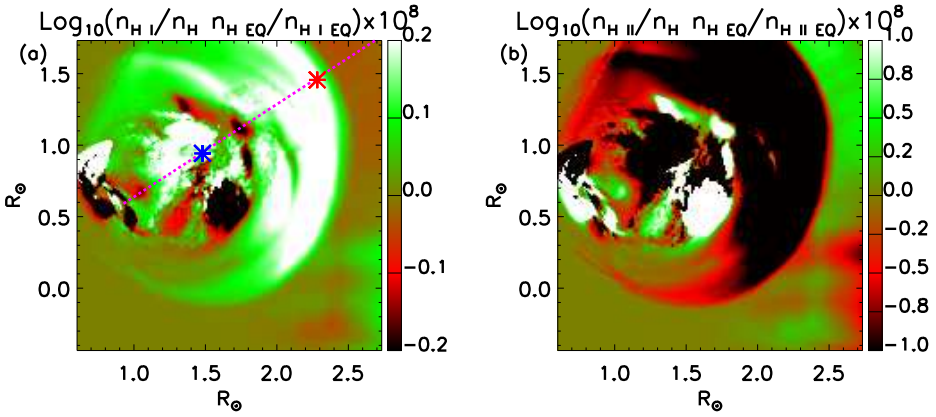

Fig. 4. Difference of the logarithms of the ionisation fraction for neutral (*a*) and ionised (*b*) hydrogen atoms with respect to the values provided under the hypothesis of ionisation equilibrium at $t = 19.7$ min. The magenta line shows the trajectory of the CME on the plane of sky. Also, the blue and red asterisks denote the positions of the magnetic flux rope and of the CME front at this time, respectively.

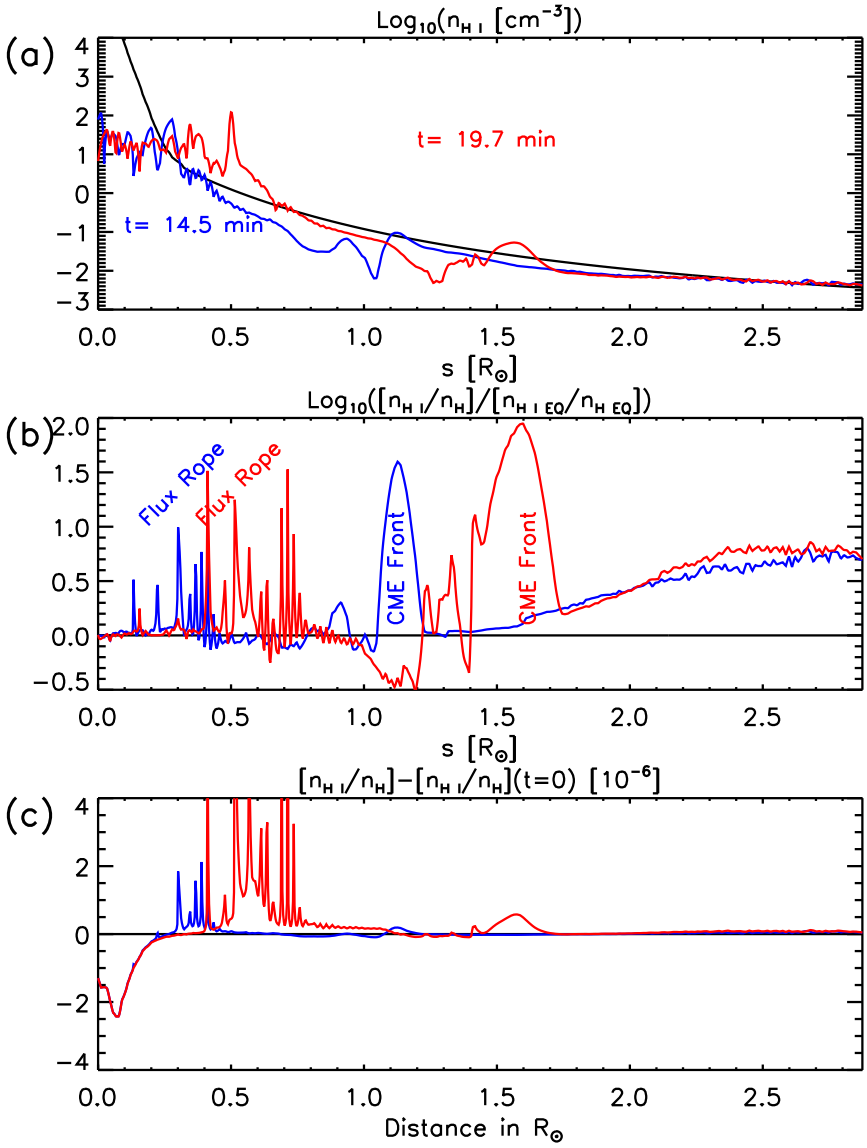

Fig. 5. (*a*) Radial profiles of neutral hydrogen atoms along the flux rope propagation direction in the pre-CME corona (black line) and during the eruption at $t = 14.5$ min (blue line) and $t = 19.7$ min (red line). (*b*) Comparison between ionisation equilibrium and non-equilibrium ionisation cases at the same times, with labelled positions of the flux rope and CME front at different times. (*c*) Changes in relative abundance of neutral hydrogen at the same cuts and the same times.

almost 100 times higher than that of ionisation equilibrium and this occurs consistently through the CME front for an extension of about $\sim 0.3\,R_\odot$. In Fig. 5c we show the change in the neutral hydrogen relative abundance along the same direction, where we find an increase of neutral hydrogen relative abundance with respect to the initial configuration at the flux rope location. As previously mentioned, this is a natural consequence of the advection of the many neutral hydrogen atoms from the initial position of the flux rope to higher altitude. A small increase is also found at the CME front locations, which is due to local velocity fields near the front.

In Fig. 6 we compare the neutral hydrogen atom abundance with the ionisation equilibrium conditions for the centre of the magnetic flux rope location and the CME front as a function of time. For the flux rope, the abundance of the neutral hydrogen atoms remains very close to those at ionisation equilibrium

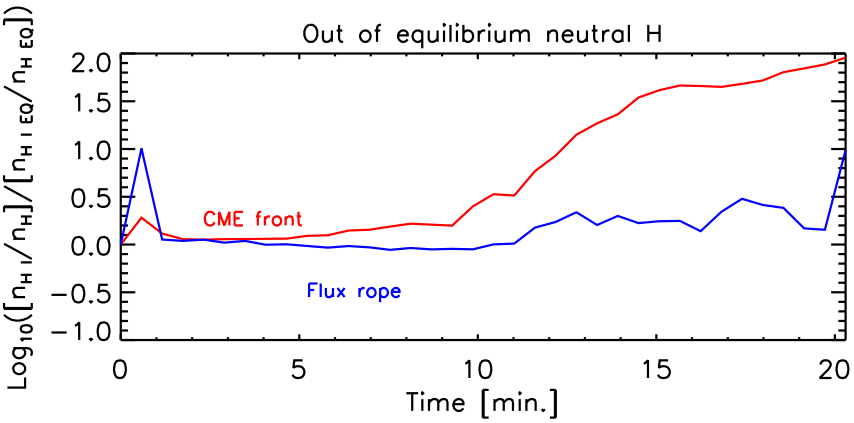

Fig. 6. Time evolution of relative abundance of neutral hydrogen atoms in the CME front (red line) and in the CME core (blue line); the curves show the comparison between the ionisation equilibrium and non-equilibrium ionisation cases at each time.

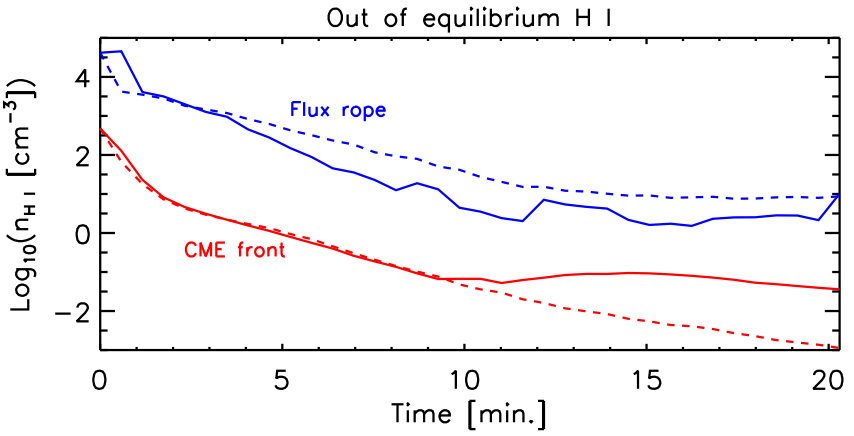

Fig. 7. Time evolution of absolute abundance of neutral hydrogen atoms in the CME front (red line) and in the CME core (blue line), with respect to the ionisation equilibrium values (dashed lines).

condition at all times, except for a very short-lived peak at the beginning of the simulation when impulsive heating occurs. This shows that the high-density conditions in the flux rope allows for a quick settlement to ionisation equilibrium. In contrast, the abundance of neutral hydrogen atoms steadily departs from ionisation equilibrium conditions as soon as a CME front develops. In our study, we followed the ionisation state of hydrogen atoms for approximately 20 min and at the end, the abundance of the neutral hydrogen atoms saturates to a value that is about 100 times higher than the abundance expected from ionisation equilibrium.

The physical explanation for this behaviour can be explained by comparing the evolution of the number of neutral hydrogen atoms in the magnetic flux rope and in the CME front as a function of time, which is shown in Fig. 7. This should be compared with Fig. 2, where we show the evolution of density and temperature in the same structures. For the centre of the magnetic flux rope, the expected density of neutral hydrogen atoms at ionisation equilibrium steadily decreases (blue dashed curve) as the plasma density there decreases faster than the temperature does. While a lower temperature would lead to more neutral hydrogen atoms, the overall lower density prescribes less particles in general. However, when we reconstruct the ionisation state of the plasma, we find fewer neutral hydrogen atoms in the magnetic flux rope (blue solid line) than at the ionisation equilibrium as the ionisation state needs to adapt while the temperature is decreasing. Also for the CME front, the expected density of neutral hydrogen atoms at ionisation equilibrium steadily decreases because of the steady decrease of the plasma density (red dashed curve), whereas the CME front temperature remains more or less constant. However, the decrease of neutral hydrogen atoms is not as rapid (red solid curve) because the front is initially loaded with a higher number of neutral hydrogen atoms and as the temperature increases, the ionisation state needs time to adapt to the changing temperature.

Figure 8 shows the relative abundance of neutral hydrogen atoms as a function of the temperature for the flux rope and the CME front. This is compared with the abundance that would be measured at the ionisation equilibrium. Although this specific estimate is highly dependent on the CME model that is used here, it still bears some interesting results, as it so happens that the flux rope is mostly near the ionisation equilibrium except in the range of $5.7 < \mathrm{Log}_{10}(T) < 5.9$. This is the temperature range in which the flux rope, shortly after the eruption when the resistive heating occurs, converges to equilibrium as it cools down. In contrast, the front remains close to ionisation equilibrium for lower temperatures $\mathrm{Log}_{10} < 6.9$ and then it significantly departs from equilibrium at higher temperatures.

It should be noted, however, that the unavoidable superposition of structures along the LOS can have a significant effect on these estimates. Figure 9 shows the number density of neutral hydrogen along the two lines of sight identified in Fig. 4; one cuts through the magnetic flux rope (Fig. 9a) and the other cuts through the CME front (Fig. 9b) and these densities are compared with the values obtained assuming ionisation equilibrium. The magnetic flux rope is much denser than other structures along the LOS; therefore, whether or not we consider the integration along the LOS does not significantly change the measured ionisation state. On the other hand, the CME front has a density that is comparable with the background density, hence the significantly higher number of neutral hydrogen atoms that we find at the front location is smoothed when the integration along the

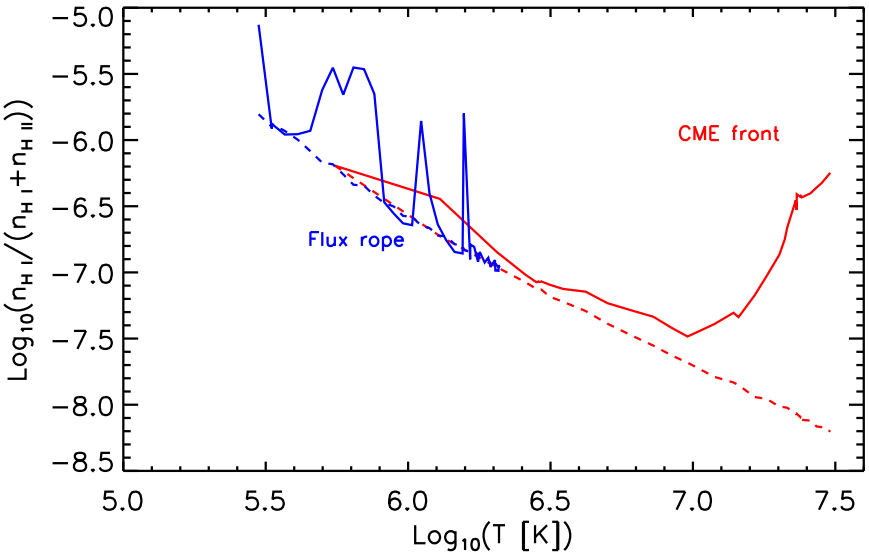

Fig. 8. Abundance of neutral hydrogen as a function of temperature for the flux rope and CME front locations.

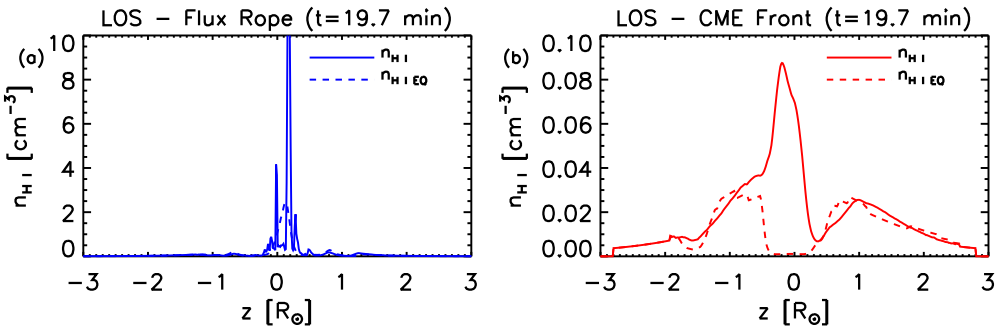

Fig. 9. (*a*) Neutral hydrogen number density along the line of sight through the magnetic flux rope (solid line) and assuming ionisation equilibrium (dashed line) at t = 19.7 min. (*b*) Neutral hydrogen number density along the line of sight through the CME front (solid line) and assuming ionisation equilibrium (dashed line) at t = 19.7 min.

LOS is considered. For this reason, the flux rope shows an abundance of neutral hydrogen atoms that is of the order of 10 times (or less) the abundance in ionisation equilibrium and the same ratio is shown when we integrate along the LOS. The CME front, instead, shows an abundance of neutral hydrogen atoms that is up to 100 times higher than the abundance in ionisation equilibrium. However, when we integrate along the LOS, the count of neutral hydrogen atoms is only about 10 times higher than the ionisation equilibrium conditions.

5. Discussion and conclusions

In this work we have used the MHD simulation of a magnetic flux rope ejection and CME propagation in the solar corona from Pagano et al. (2014) to study the abundances of ionised and neutral hydrogen atoms during CMEs. In particular, we focus on the non-equilibrium ionisation effects in order to verify to what extent the assumption of ionisation equilibrium holds during these phenomena. This work is especially important for the forthcoming measurements of Metis, the coronagraph on board the Solar Orbiter mission, and LST, the coronagraph on board ASO-S, which will observe the solar corona in the Lyman-α line that is produced by neutral hydrogen atoms. A number of measurements of plasma properties, such as the plasma temperature, crucially depend on the number of neutral hydrogen atoms and on the assumptions that have been made for the ionisation state of the plasma. For example, one way to derive the plasma temperature is to compare the abundances of neutral and ionised hydrogen atoms and to find the temperature at which the measured abundances are in agreement with the theoretical ones estimated by the ionisation equilibrium hypothesis. These kinds of derivations are inherently prone to errors if the plasma is not in ionisation equilibrium. To this end, this work sheds light on the regions and phenomena that occur when the assumption of ionisation equilibrium holds and when it does not.

In order to reconstruct the ionisation state of hydrogen atoms during a CME propagation in the solar corona, we used the MHD simulation of Pagano et al. (2014) that provides the 3D plasma density and temperature distributions as a function of time, together with the plasma velocity fields. Using these as inputs and assuming ionisation equilibrium at the beginning of the CME propagation, we devised a technique to solve the differential equations that describe the change in the number of neutral and ionised hydrogen atoms as a function of space and time, using the strategy already introduced in Pagano et al. (2008). More specifically, we estimated the advection as well as the ionisation and recombination terms separately in order to express the rate of change of the number of ionised and neutral hydrogen atoms in one cell of the MHD simulation. By time-integrating the rate of change, we can describe abundance of neutral and ionised hydrogen atoms as a function of space and time in our MHD simulation. This technique bears no assumption on the ionisation state of the plasma and it can describe abundances of ionised and neutral hydrogen atoms out of ionisation equilibrium.

Finally, to analyse the results of this study with regards to the temperature measurements in the solar corona, we have compared the obtained distributions of neutral and ionised hydrogen atoms with respect to the distributions associated with ionisation equilibrium. We did this through the entire 3D domain of the MHD simulation and specifically for the centre of the magnetic flux rope and the CME front, which are two prominent features of CMEs.

We find that the departures from ionisation equilibrium are negligible for the abundance of ionised hydrogen atoms, where any departure is small enough to become irrelevant, as the vast majority of hydrogen atoms are ionised in the solar corona. However, this is not the case for neutral hydrogen since there are inherently few of these atoms in the corona and, therefore, small variations can lead to a significant departure from the assumed abundance at ionisation equilibrium. We crucially find that non-equilibrium ionisation effects for neutral hydrogen atoms are marginal for the regions pertinent to the magnetic flux rope. This means that the number of neutral hydrogen atoms in the magnetic flux rope is generally consistent with the number one would assume in ionisation equilibrium conditions. Although we observe some small-scale variations and rapid changes from one location to another within the magnetic flux rope, overall we find that these effects are not detectable when the whole flux rope is considered. This means that for the future derivation of plasma temperatures based on observed Lyman-α line intensities, the ionisation equilibrium hypothesis is still applicable.

In contrast, we find that non-equilibrium ionisation effects are relevant at the CME front, where the number of neutral hydrogen is much higher than the expected abundance from the assumption of ionisation equilibrium conditions. We find this to be consistent over the whole extension of the CME front and that the departure is as large as 2 orders of magnitude in excess with respect to the ionisation equilibrium conditions. In the region where we have an excess of neutral hydrogen atoms, the derived temperature from the abundances would be much lower than the actual temperature value, and thus using the ionisation equilibrium assumption would lead to a significant plasma temperature underestimate at the CME front. At the same time, we also find that the projection effect along the LOS can partially hide these effects as it happens here for the CME front where non-equilbrium ionisation effects are smoothed out after the integration along the LOS and the superposition of structures in ionisation equilibrium that have comparable densities.

In the future, more studies need to be carried out to investigate the parameter space of the CME velocities, densities, and temperatures, along with considering more diverse configurations of the magnetic flux rope ejections. It is also important to apply this approach (the magnetofrictional simulation, the MHD simulation, and the reconstruction of the ionisation state of the hydrogen atoms) to observed events to more accurately verify these results. In particular, the analysis carried out in Fig. 8 can potentially be extended to many more cases where MHD simulations can be used to derive a more accurate and reliable lookup table to invert the temperature of CME fronts and cores as a function of the relative abundance of neutral hydrogen. At the same time, this work already provides key information for a correct interpretation of future plasma properties derived from Lyman-α observations, which is certainly crucial for the future observations of Metis on board Solar Orbiter and LST on board ASO-S telescopes.

Acknowledgements. This research has received funding from the Science and Technology Facilities Council (UK) through the consolidated grant ST/N000609/1 and the European Research Council (ERC) under the European Union Horizon 2020 research and innovation program (grant agreement No. 647214). D.H.M. would like to thank both the UK STFC and the ERC (Synergy grant: WHOLE SUN, grant Agreement No. 810218) for financial support. D.H.M. and P.P. would like to thank STFC for IAA funding under grant number SMC1-XAS012. This work used the DiRAC@Durham facility managed by the Institute for Computational Cosmology on behalf of the STFC DiRAC HPC Facility (www.dirac.ac.uk). The equipment was funded by BEIS capital funding via STFC capital grants ST/P002293/1, ST/R002371/1 and ST/S002502/1, Durham University and STFC operations grant ST/R000832/1. DiRAC is part of the National e-Infrastructure. We acknowledge the use of the open source (gitorious.org/amrvac) MPI-AMRVAC software, relying on coding efforts from C. Xia, O. Porth, R. Keppens. CHIANTI is a collaborative project involving George Mason University, the University of Michigan (USA), University of Cambridge (UK) and NASA Goddard Space Flight Center (USA).

References

Akmal, A., Raymond, J. C., Vourlidas, A., et al. 2001, ApJ, 553, 922
Antonucci, E., Andretta, V., Cesare, S., et al. 2017, Proc. SPIE, 10566, 105660L
Aschwanden, M. J. 2017, ApJ, 847, 27
Bemporad, A., & Pagano, P. 2015, A&A, 576, A93
Bemporad, A., Pagano, P., & Giordano, S. 2018, A&A, 619, A25
Bradshaw, S. J. 2009, A&A, 502, 409
Bradshaw, S. J., & Testa, P. 2019, ApJ, 872, 123
Chen, P. F. 2011, Liv. Rev. Sol. Phys., 8, 1
Cheng, X., Ding, M. D., & Zhang, J. 2010, ApJ, 712, 1302
Ciaravella, A., Raymond, J. C., Reale, F., Strachan, L., & Peres, G. 2001, ApJ, 557, 351
Ciaravella, A., Raymond, J. C., & Kahler, S. W. 2006, ApJ, 652, 774
Colgan, J., Abdallah, J., Sherrill, M. E., et al. 2008, ApJ, 689, 585
Courant, R., Friedrichs, K., & Lewy, H. 1928, Math. Ann., 100, 32
Dere, K. P., Del Zanna, G., Young, P. R., Landi, E., & Sutherland, R. S. 2019, ApJS, 241, 22
Dudík, J., Janvier, M., Aulanier, G., et al. 2014, ApJ, 784, 144
Dudík, J., Dzifčáková, E., Meyer-Vernet, N., et al. 2017, Sol. Phys., 292, 100
Frassati, F., Susino, R., Mancuso, S., & Bemporad, A. 2019, ApJ, 871, 212
Godunov, S. 1959, Math. Sbornik, 47, 271
Hannah, I. G., & Kontar, E. P. 2013, A&A, 553, A10
Howard, T. A., & DeForest, C. E. 2014, ApJ, 796, 33
Imada, S., Hara, H., Watanabe, T., et al. 2011, ApJ, 743, 57
Jejčič, S., Susino, R., Heinzel, P., et al. 2017, A&A, 607, A80
Karlický, M., Kašparová, J., & Heinzel, P. 2004, A&A, 416, L13
Kocher, M., Landi, E., & Lepri, S. T. 2018, ApJ, 860, 51
Landi, E., Raymond, J. C., Miralles, M. P., & Hara, H. 2010, ApJ, 711, 75
Lee, J.-Y., Raymond, J. C., Reeves, K. K., et al. 2019, ApJ, 879, 111
Li, H. 2016, IAU Symp., 320, 436
Mackay, D. H., & van Ballegooijen, A. A. 2006, ApJ, 641, 577
Mackay, D. H., Green, L. M., & van Ballegooijen, A. 2011, ApJ, 729, 97
Martínez-Sykora, J., De Pontieu, B., Hansteen, V. H., & Gudiksen, B. 2016, ApJ, 817, 46
Murphy, N. A., Raymond, J. C., & Korreck, K. E. 2011, ApJ, 735, 17
Noci, G., Kohl, J. L., & Withbroe, G. L. 1987, ApJ, 315, 706
Pagano, P., Raymond, J. C., Reale, F., & Orlando, S. 2008, A&A, 481, 835
Pagano, P., Mackay, D. H., & Poedts, S. 2013a, A&A, 554, A77
Pagano, P., Mackay, D. H., & Poedts, S. 2013b, A&A, 560, A38
Pagano, P., Mackay, D. H., & Poedts, S. 2014, A&A, 568, A120
Pagano, P., Bemporad, A., & Mackay, D. H. 2015a, A&A, 582, A72
Pagano, P., Mackay, D. H., & Poedts, S. 2015b, JApA, 36, 123
Pagano, P., Mackay, D. H., & Yeates, A. R. 2018, J. Space Weather Space Clim., 8, A26
Porth, O., Xia, C., Hendrix, T., Moschou, S. P., & Keppens, R. 2014, ApJS, 214, 4
Raymond, J. C., Ghavamian, P., Sankrit, R., Blair, W. P., & Curiel, S. 2003, ApJ, 584, 770
Reep, J. W., Bradshaw, S. J., Crump, N. A., & Warren, H. P. 2019, ApJ, 871, 18
Rodkin, D., Goryaev, F., Pagano, P., et al. 2017, Sol. Phys., 292, 90
Shen, C., Reeves, K. K., Raymond, J. C., et al. 2013, ApJ, 773, 110
Shen, C., Raymond, J. C., Mikić, Z., et al. 2017, ApJ, 850, 26
Shi, T., Landi, E., & Manchester, W. I 2019, ApJ, 882, 154
Smith, R. K., & Hughes, J. P. 2010, ApJ, 718, 583
Song, H. Q., Zhang, J., Chen, Y., & Cheng, X. 2014, ApJ, 792, L40
Spitzer, L. 1962, Physics of Fully Ionized Gases, 2nd edn. (New York: Interscience)
Su, W., Cheng, X., Ding, M. D., et al. 2016, ApJ, 830, 70
Susino, R., & Bemporad, A. 2016, ApJ, 830, 58
Yan, X. L., Jiang, C. W., Xue, Z. K., et al. 2017, ApJ, 845, 18
Ying, B., Bemporad, A., Giordano, S., et al. 2019, ApJ, 880, 41